Finite-temperature simulation of anharmonicity and octahedral tilting transitions in halide perovskites

Jonathon S. Bechtel, John C. Thomas,* and Anton Van der Ven†
Materials Department, University of California, Santa Barbara, Santa Barbara, California 93106, USA

(Received 12 August 2019; published 18 November 2019)

Octahedral tilting transitions are observed in most inorganic halide perovskites and play an important role in determining their functional and thermodynamic properties. Despite existing near room temperature, the cubic and tetragonal forms of halide perovskites become dynamically unstable at low temperature, making it impossible to study their thermodynamic properties with commonly used quasiharmonic models. An anharmonic vibrational Hamiltonian is constructed that accurately reproduces the low-energy portion of the potential-energy surface of the halide perovskite $CsPbBr_3$. The Hamiltonian is validated using a large first-principles dataset of energies calculated within density functional theory for large-amplitude deformations of the $CsPbBr_3$ crystal. Monte Carlo simulations performed on the Hamiltonian reproduce the orthorhombic-tetragonal-cubic phase transitions observed in $CsPbBr_3$ and many other halide perovskites, demonstrating the importance of anharmonic vibrational excitations in stabilizing the tetragonal and cubic phases in these materials. Measures of local structure and octahedral tilting in the cubic and tetragonal phases, obtained from Monte Carlo simulations, confirm the connection between large anisotropic displacement factors and octahedral tilting, as observed experimentally.

DOI: 10.1103/PhysRevMaterials.3.113605

I. INTRODUCTION

The past decade has seen impressive increases in power conversion efficiencies of halide perovskite-based photovoltaic devices [1]. Halide perovskites differ from most other electronic materials in that their unique electronic properties are strongly affected by vibrational excitations. Their soft anharmonic crystals result in Rashba-Dresselhaus splitting of the conduction band [2–7] and give rise to strong electron-phonon interactions that allow for large polaron formation [8–10]. Anharmonic vibrational excitations also play a key role in the structural phase transitions of halide perovskites. Most halide perovskites undergo a series of group/subgroup structural phase transitions upon cooling as a result of symmetry-breaking octahedral tilts. The inorganic $CsPbBr_3$ perovskite, for example, is stable in the cubic $Pm\bar{3}m$ phase at elevated temperature but transforms to a tetragonal phase having $P4/mbm$ symmetry at intermediate temperature and an orthorhombic phase with $Pnma$ symmetry at very low temperatures [11–19].

The cubic and tetragonal forms of halide perovskites distinguish themselves from most other room-temperature phases in that they are usually dynamically unstable at zero Kelvin with respect to octahedral tilt modes [5,14,20–25]. Figure 1, for example, shows an energy landscape, as calculated with an approximation to density functional theory, of $CsPbBr_3$ in the perovskite crystal structure as a function of two collective octahedral tilt modes [20]. The cubic form, referred to as α, resides at the origin in Fig. 1 and its energy corresponds to a local maximum. The tetragonal phase β is obtained from the cubic phase by the activation of in-phase tilt modes about the z-rotation axis with amplitude a, denoted $(00a^+)$ in Glazer notation [26]. Its energy is a saddle point. The low-temperature orthorhombic phase γ emerges from the tetragonal phase by the activation of two simultaneous antiphase tilts about the x and y rotation axes, resulting in the $(b^-b^-a^+)$ tilt pattern. As is clear from Fig. 1, only the orthorhombic phase resides in an energy well. The negative curvatures in the energy landscape for the cubic and tetragonal symmetries show that these phases are dynamically unstable and cannot be described with harmonic vibrational Hamiltonians, where the potential energy is expanded to only second order in terms of atomic displacements. The emergence of the cubic and tetragonal forms of $CsPbBr_3$ at elevated temperature must therefore arise from large anharmonic vibrational excitations.

Several approaches exist to model anharmonic lattice dynamics and temperature-dependent structural phase transitions. A direct approach is to perform *ab initio* molecular dynamics (AIMD) simulations to calculate thermodynamic averages as a function of temperature [25,27–29]. AIMD, however, is computationally expensive and limited to short times and small supercell sizes. Approaches that rely on self-consistent [30] or constrained [31,32] extensions of harmonic phonon analyses have shown promise for approximating the free energies of anharmonically stabilized phases, although at the expense of discarding information about dynamical phenomena in the high-temperature phase. Still other approaches rely on anharmonic effective Hamiltonians to interpolate and extrapolate expensive first-principles calculations within large-scale Monte Carlo simulations. These were developed

*johnct@engineering.ucsb.edu
†avdv@engineering.ucsb.edu

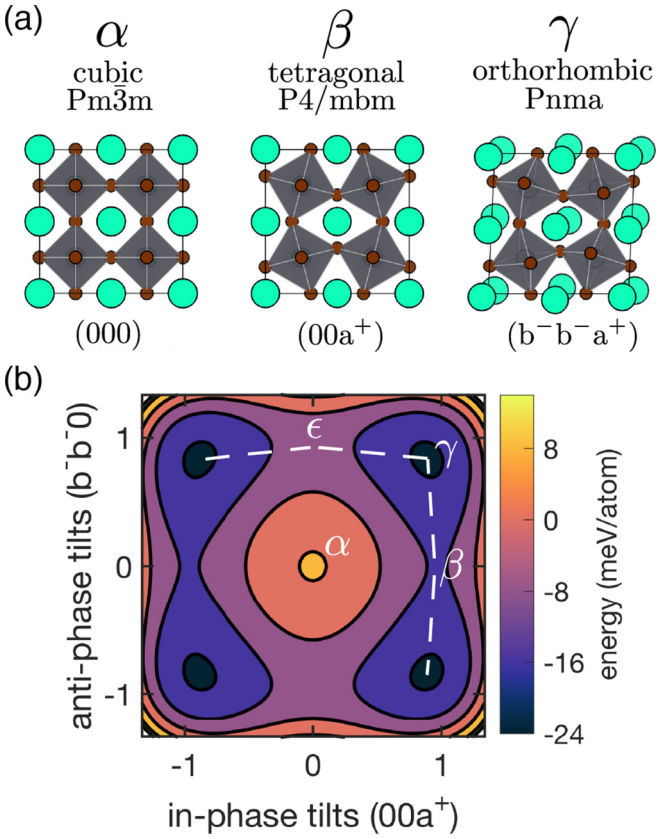

FIG. 1. (a) Many halide perovskites such as $CsPbBr_3$ undergo a series of structural transitions upon cooling, starting in a cubic form at high temperature and transforming to tetragonal and orthorhombic forms at low temperature as a result of octahedral tilts. (b) The energy surface of $CsPbBr_3$ as a function of octahedral tilts, calculated with density functional theory for configurations with orthorhombic lattice parameters. For each configuration, the $PbBr_6$ sublattice and lattice parameters were held fixed while the Cs sublattice was allowed to relax. The energy surface shows that the cubic phase α coincides with a local maximum, the tetragonal phase β resides at a saddle point, and the ground-state orthorhombic phase γ corresponds to a stable minimum. (Crystal structures are visualized using the VESTA program suite [50].)

early on to study polar and octahedral tilt distortions in oxide perovskites [33–45] and have been refined in recent years to study other classes of group/subgroup structural phase transitions [46–49].

The aim of this study is to elucidate the group/subgroup structural phase transitions involving octahedral tilts in inorganic halide perovskites. To this end, we develop a minimal anharmonic vibrational Hamiltonian that captures the essential physics of the orthorhombic to tetragonal to cubic structural transitions of inorganic halide perovskites such as $CsPbBr_3$. We parametrize the Hamiltonian to approximate the first-principles potential-energy surface of $CsPbBr_3$ near its observed perovskite phases to develop a model that faithfully reproduces the dynamical instabilities exhibited by common halide perovskites. We then explore the finite temperature behavior of this Hamiltonian with Monte Carlo simulations and demonstrate that the cubic and tetragonal phases emerge at elevated temperature, in spite of the fact that they reside at local maxima or saddle points on the zero-Kelvin energy landscape. The use of a minimal anharmonic vibrational Hamiltonian allows us to parametrically isolate the role of particular interactions in affecting the nature of structural phase transitions in halide perovskites due to octahedral tilt modes. We explore how small changes in the energy surface of Fig. 1 manifest themselves in the finite temperature behavior and find that changes in the interaction strength between halides of neighboring octahedra can have a strong influence on the finite temperature stability of the intermediate tetragonal form.

II. METHOD

We express the potential-energy surface of a crystal as a sum of contributions due to individual clusters of sites, according to [51]

$$E(\ldots,\vec{u}_i,\ldots) = E_0 + \sum_\alpha \Phi_\alpha\left(q_1^\alpha,\ldots,q_{n_\alpha}^\alpha\right). \tag{1}$$

E_0 is the energy of a specified reference crystal, and the $\vec{u}_i$ are displacement vectors of the sites i relative to their position in the reference crystal. The contribution from a cluster α is a function of variables $q_1^\alpha,\ldots,q_{n_\alpha}^\alpha$ that measure the degree to which the cluster is distorted relative to its state in the reference crystal. The set of clusters $\{\alpha\}$ typically comprise pair clusters and compact multibody clusters such as tetrahedra and octahedra. Defining the variables $q_1^\alpha,\ldots,q_{n_\alpha}^\alpha$ to be invariant to rigid translations and rotations of the distorted cluster ensures that the energy expression is itself invariant to rigid translations and rotations of the crystal. In studying group/subgroup structural phase transitions, it is common to use the high-symmetry phase as the reference crystal. The symmetry of the reference crystal then imposes additional constraints on the cluster functions Φ_α to ensure that any two displacement fields that are equivalent under a symmetry operation of the reference crystal have the same energy.

There are multiple ways to arrive at variables that rigorously describe deformations of a cluster α relative to its undistorted shape in a reference crystal [47,51]. One is to rely on distances, d_l, between each constituent pair, l, of sites within cluster α in its deformed state. Each pair distance d_l is invariant to rigid translations and rotations of cluster α, and knowledge of all pair distances of a cluster is sufficient to reconstruct the cluster up to a rigid translation and rotation. Since we are interested in deformations of a cluster relative to its undistorted state in a reference crystal, it is more convenient to work with functions of pair distances $f(d_l)$ that are zero in the reference state. Several possible functional forms for f include

$$f_{\text{lin}} = \sqrt{\frac{d_l^2}{\tilde{d}_l^2}} - 1\,, \tag{2}$$

$$f_{\text{quad}} = \frac{1}{2}\left(\frac{d_l^2}{\tilde{d}_l^2} - 1\right), \tag{3}$$

$$f_{\text{log}} = \frac{1}{2}\ln\frac{d_l^2}{\tilde{d}_l^2}\,, \tag{4}$$

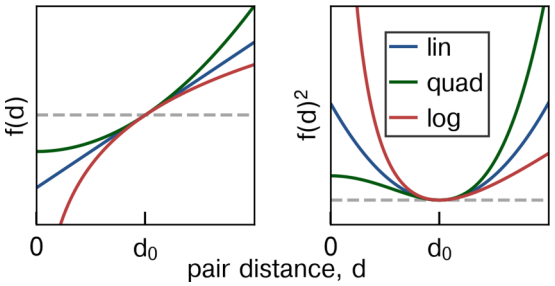

FIG. 2. (a) Linear (blue), quadratic (green), and logarithmic (red) pair functors plotted as a function of pair distance. The reference pair distance is denoted as d_0, and the dotted line represents $f(d) = 0$. (b) The square of the different pair functors are plotted. The log functor is used in this study in order to penalize pair contraction over pair expansion giving rise to volumetric expansion upon heating.

where $\tilde{d}_l$ represents the reference pair distance. A suitable pair-deformation function satisfies three constraints: (1) f is monotonic; (2) the slope of f at $d_l = \tilde{d}_l$ is $1/\tilde{d}_l$; and (3) $f(\tilde{d}_l) = 0$. As is evident from Fig. 2, the log function is particularly useful to model the energy of a crystal since it penalizes pair contraction more heavily than pair expansion, thereby naturally accounting for the typical behavior of solids to become softer upon volumetric expansion.

While the $f(d_l)$ evaluated for all constituent pairs of the cluster could by themselves serve as descriptors of the cluster deformation, it is more convenient to work with collective cluster deformation (CCD) variables, which are symmetry-adapted linear combinations of the $f(d_l)$ according to

$$q_k = \sum_l U_{kl} f(d_l). \tag{5}$$

The U_{kl} are elements of a matrix $\mathbf{U}$ that transforms a vector having elements $\{f(d_l)\}$ to a new vector $\vec{Q}^\alpha = (q_1^\alpha, \ldots, q_k^\alpha \ldots)$ representing collective distortions of the cluster α. The matrix $\mathbf{U}$ is chosen such that the resulting CCD variables can be grouped into distinct subspaces corresponding to irreducible representations (irreps) of the cluster point group $\mathcal{P}^\alpha$ (this is the subgroup of the crystal space group that maps the reference cluster α onto itself). As an example, Fig. 3 illustrates the CCDs generated in this manner for an octahedral cluster and a pair cluster. The octahedron CCDs q_1, q_2, and q_3 of Fig. 3, for instance, define a three-dimensional CCD subspace corresponding to an individual irrep. A symmetry operation acting on a CCD vector within this subspace can map it to a new vector within the subspace having the same length, but it cannot map it to a new vector having a component corresponding to any other irreducible representation. Similarly, any volumetric deformation is completely encompassed by the one-dimensional irrep corresponding to the q_0 CCD. Detailed definitions of the octahedral CCD variables, including the geometry of the undeformed reference cluster, are provided in the Supplemental Material [52].

With robust collective cluster deformation variables that are both translation and rotation invariant, we next establish a functional form for the cluster functions Φ_α of Eq. (1). Similar to the anharmonic vibrational cluster expansion [47], we express Φ_α as a linear expansion of polynomials of

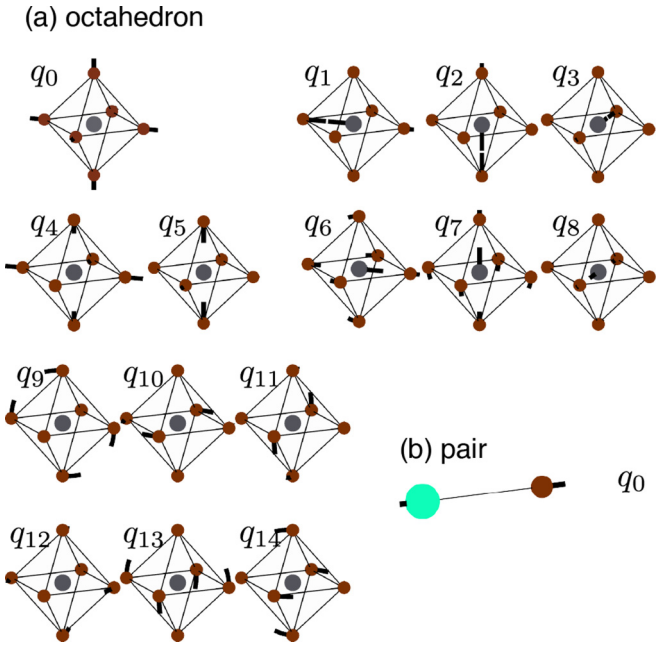

FIG. 3. Collective cluster deformations (CCDs) for (a) an octahedron and (b) a pair. The octahedral CCDs are organized by irreducible representations, with one 1D irrep, one 2D irrep, and four 3D irreps. A pair cluster has only one CCD corresponding to the pair distance.

$\vec{Q}^\alpha = q_1^\alpha, \ldots, q_{n_\alpha}^\alpha$ according to

$$\Phi_\alpha(\vec{Q}^\alpha) = \sum_n V_n^\alpha \phi_n^\alpha(\vec{Q}^\alpha), \tag{6}$$

where V_n^α are expansion coefficients, referred to as effective cluster interactions (ECI), that are determined by the chemistry of the crystal, and $\phi_n^\alpha(\vec{Q}^\alpha)$ are polynomials of the elements of $\vec{Q}^\alpha$. The polynomials must be invariant to the symmetry of the cluster within the reference crystal. For instance, although the second-order functions q_1^2, q_2^2, and q_3^2 of the octahedron cluster are *not* symmetry invariant, the function $(q_1^2 + q_2^2 + q_3^2)$ *is* symmetry invariant, since deformations along q_1, q_2, and q_3 are related by symmetry. A complete set of polynomials $\{\phi_n^\alpha(\vec{Q})\}$ that are invariant to the relevant symmetries of the parent phase can be constructed systematically using the Reynold's operator, as described in Ref. [47].

In general, it is necessary to include several different cluster types in the expansion of Eq. (1). For the perovskite crystal structure, for example, a minimal Hamiltonian should include the octahedron, along with a variety of pairs not already included in the octahedron. All clusters β that can be mapped onto a prototype cluster α by a symmetry operation of the parent crystal structure are said to belong to the orbit of α, denoted as Ω_α. Any two cluster functions ϕ_n^β and $\phi_n^{\beta'}$ corresponding to clusters belonging to the same orbit, Ω_α, have the same set of expansion coefficients V_n^α. The total energy of the crystal can then be expressed as

$$E(\ldots, \vec{u}_i, \ldots) = E_0 + \sum_\alpha \sum_{\beta \in \Omega_\alpha} \sum_n V_n^\alpha \phi_n^\beta(\vec{Q}^\beta), \tag{7}$$

where α indexes the unique cluster types, β indexes the symmetrically equivalent clusters within the orbit Ω_α, and n

TABLE I. Basis functions and fitting coefficients as parametrized from the neural-network model.

Cluster function	ECI[a]	ECI value (meV)	Basis function
Φ_{CsBr}	V_0	70.035	q_0
	V_1	−14.314	q_0^2
	V_2	−19.616	q_0^3
	V_3	9.093	q_0^4
Φ_{CsPb}	V_0	−4.236	q_0
	V_1	11.276	q_0^2
Φ_{BrBr}	V_0	−3.620	q_0
	V_1	8.687	q_0^2
Φ_{CsCs}	V_0	−24.677	q_0
	V_1	49.844	q_0^2
Φ_{PbBr_6}	V_0	−267.550	q_0
	V_1	215.810	q_0^2
	V_2	−32.585	q_0^3
	V_3	5.605	q_0^4
	V_4	157.590	$q_1^2+q_2^2+q_3^2$
	V_5	23.388	$(q_1^2+q_2^2+q_3^2)^2$
	V_6	121.620	$q_4^2+q_5^2$
	V_7	6.324	$(q_4^2+q_5^2)^2$
	V_8	25.468	$q_6^2+q_7^2+q_8^2$
	V_9	0.986	$(q_6^2+q_7^2+q_8^2)^2$
	V_{10}	16.996	$q_9^2+q_{10}^2+q_{11}^2$
	V_{11}	0.102	$(q_9^2+q_{10}^2+q_{11}^2)^2$
	V_{12}	7.177	$q_{12}^2+q_{13}^2+q_{14}^2$
	V_{13}	0.045	$(q_{12}^2+q_{13}^2+q_{14}^2)^2$

[a]ECI stands for effective cluster interaction.

indexes the basis functions for that type of cluster, α. In principle, there are an infinite number of basis functions per cluster, but, in practice, only basis functions up to second, fourth, or sixth order are used. An example of the basis functions ϕ_n^α and fitting coefficients used in this study are presented in Table I. The expansion coefficients V_n^α can be determined by training the energy expression, Eq. (7), to a large dataset of energies calculated for many different distorted states of the crystal.

III. RESULTS

A. Anharmonic vibrational cluster expansion model for perovskites

We formulated a model Hamiltonian for $CsPbBr_3$ within the anharmonic potential cluster-expansion framework [47] as a linear expansion of polynomial basis functions according to Eq. (7). The minimal anharmonic vibrational Hamiltonian was constructed starting from a neural-network model of the $CsPbBr_3$ potential-energy surface described in Ref. [51]. Each cluster-based interaction in that model is computed via an artificial neural network, which is a hierarchical model comprising layers of simple nonlinear functions weighted by free parameters. The free parameters can be adjusted to approximate arbitrary functions, allowing high fidelity to the training data, though with nontrivial computational overhead and a tendency towards overfitting. Details of how various neural-network architectures may be formulated for a crystalline system are provided in Ref. [51].

We parametrized the minimal anharmonic vibrational Hamiltonian utilized in this work by fitting the polynomial interaction of each cluster to data generated by its corresponding neural network from [51]. In doing so, we obtain a computationally efficient energy expression that captures salient features of the potential-energy surface of $CsPbBr_3$ while avoiding overfitting. The error of the resulting Hamiltonian was tested against the validation set of over 30 000 density functional theory (DFT)-calculated energies utilized to train the original neural-network model [53]. This procedure resulted in a model with total root-mean-square error of 0.0277 eV/atom for all validation samples and of 0.0024 eV/atom for validation samples having DFT-calculated energies below the reference cubic energy. The CASM library was employed for constructing symmetry-invariant basis functions and parametrizing the anharmonic vibrational Hamiltonian [47,54–56].

The results of the fitting procedure are the effective cluster interaction coefficients listed in Table I. The anharmonic vibrational Hamiltonian includes terms for the $PbBr_6$ octahedron cluster and for four pair clusters: Cs−Br, Cs−Pb, Cs−Cs, and Br−Br. Several polynomial basis functions in terms of the cluster CCDs are included for each cluster. As shown in Table I, the nearest-neighbor CsBr pair energy and the octahedral cluster energy were expanded to fourth order in terms of their CCDs, while the remaining pairs were expanded only to second order. Figures 4(a)–4(e) show the clusters that are included in the anharmonic vibrational Hamiltonian along with depictions of their contribution to the total energy as a function of q_0, which is a measure of a symmetry-invariant deformation of each cluster.

Figure 5 shows that the anharmonic vibrational Hamiltonian reproduces many of the qualitative features of the DFT energy surface of $CsPbBr_3$ within the subspace of octahedral tilt modes that connect γ, β, and α (fixing the unit-cell dimensions to those of the orthorhombic unit cell). The Hamiltonian, based upon only four pairs and one octahedral cluster, is capable of reproducing the minima corresponding to orthorhombic γ, the saddle point for tetragonal β, and the local maximum for cubic α. Furthermore, it also correctly predicts a saddle point for the orthorhombic distortion corresponding to the ϵ phase, which, in a manner that is similar to tetragonal β, separates pairs of translational variants of the ground-state γ phase. The energy of this saddle point, however, is overestimated by 7.6 meV/atom relative to the DFT-calculated value. At regions of large tilts the minimal anharmonic model severely overestimates the energy. This is likely an artifact of fitting only to deformations near the minima, thereby resulting in an overestimation of the energy for large deformations. The comparison in Fig. 5 shows that the anharmonic cluster expansion qualitatively reproduces the DFT energy landscape in a small, but important subspace of all possible vibrational excitations that are possible relative to a cubic perovskite crystal. We emphasize that the validation dataset includes a large number of energies corresponding to homogeneous distortions and internal displacements that reside outside of the subspace shown in Fig. 5. More details can be found in Ref. [51].

B. Finite temperature properties

The energy surface of Fig. 1 gives preliminary insights about the types of structural phase transitions that can occur

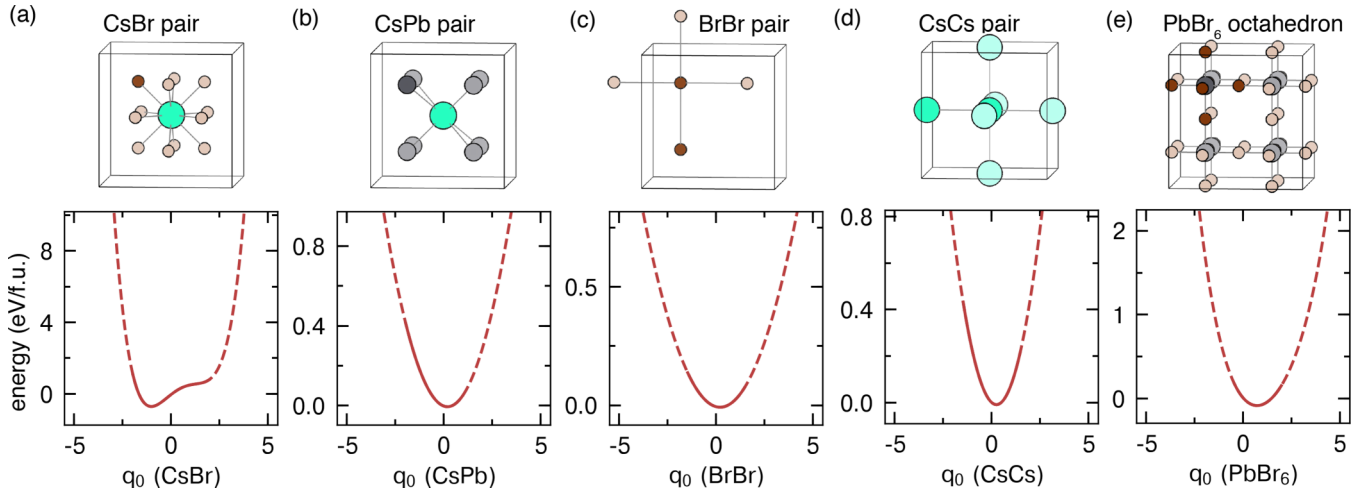

FIG. 4. (a)–(e) Symmetrically equivalent clusters (top panel) and evaluated cluster energy function (bottom panel) as a function of q_0 (volumetric deformation) for each cluster included in the anharmonic vibrational Hamiltonian.

as a function of temperature. At low temperatures, the crystal will sample states within an energy well corresponding to the orthorhombic γ-phase ground state. Figure 1 shows four of these energy wells corresponding to the translational variants of the same orthorhombic orientational variant, of which there are six [20]. At sufficiently low temperatures, the vibrational excitations are harmonic and restricted to the bottom of one of the wells. Upon heating, the crystal is able to sample more energetically unfavorable states. The shallow and highly anharmonic energy surface of Fig. 1 indicates that anharmonic vibrational excitations should already become important at low temperatures. Above a particular temperature, there is sufficient thermal energy for the crystal to no longer be constrained to a single orthorhombic well. Figure 1 shows the existence of shallow valleys connecting pairs of translational variants of γ with a tetragonal β residing at a saddle point separating each pair of γ variants. We can expect the emergence of an averaged crystal having tetragonal β symmetry once the available thermal energy allows the crystal to escape a particular orthorhombic well of Fig. 1. At even higher temperature, the crystal is able to escape the valley centered around the tetragonal β symmetry and start sampling a larger part of phase space that has on average cubic symmetry.

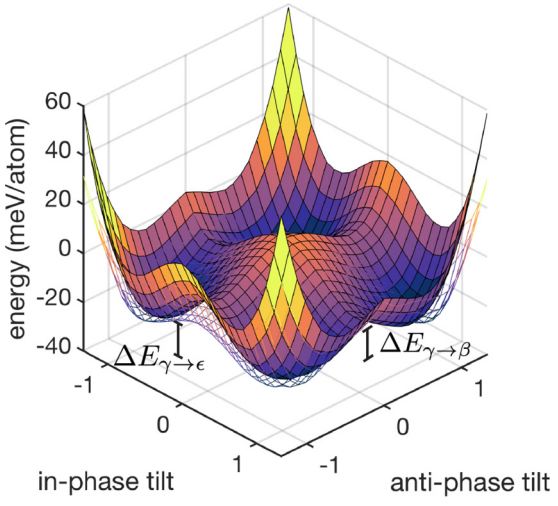

FIG. 5. Potential energy landscape of the minimal anharmonic vibrational Hamiltonian (solid) compared to the DFT energy landscape (mesh). Energy barriers through the ϵ phase and β phases are depicted and labeled $\Delta E_{\gamma\to\epsilon}$ and $\Delta E_{\gamma\to\beta}$, respectively. The minimal Hamiltonian reproduces many of the qualitative features of the DFT energy landscape; however, it overestimates the energy barrier $\Delta E_{\gamma\to\epsilon}$.

It is important to note that the energy surface in Fig. 1 represents homogenous deformations to the crystal, while a real crystal will sample a much higher dimensional space of microstates, since each local environment is free to sample states relatively independently of other local environments. The anharmonic vibrational Hamiltonian allows us to sample this high-dimensional space of microstates within Monte Carlo simulations where thermodynamic averages and local correlations can be calculated. These averages provide insight about the nature of anharmonic vibrations that stabilize the tetragonal and cubic phases at elevated temperature.

Finite temperature Monte Carlo simulations using the Metropolis-Hastings algorithm were performed on the anharmonic cluster expansion to investigate structural phase transitions as a function of temperature. During each Monte Carlo pass, atomic displacement perturbations and homogenous strain perturbations were proposed such that, on average, each site in the crystal is visited once. Strain perturbations were proposed in a ratio of 1:100 to atomic perturbations. Thermodynamic averages are computed once the system has equilibrated, typically around 2000–4000 passes, and averages were taken for 4000 passes. Monte Carlo simulations were initialized at low temperature with the ground-state structure. Thermodynamic averages of the deformation tensor, $\langle F \rangle$, from which strains can be calculated [47,57], and atomic displacements, $\langle \vec{u} \rangle$, were used to analyze the evolution of local and average structure as a function of temperature. Simulations were performed in a 8,640-atom $12 \times 12 \times 12$ supercell of the $CsPbBr_3$ primitive cell, except where noted.

Figure 6 shows the temperature dependence of averaged strain order parameters [58] as calculated with Monte

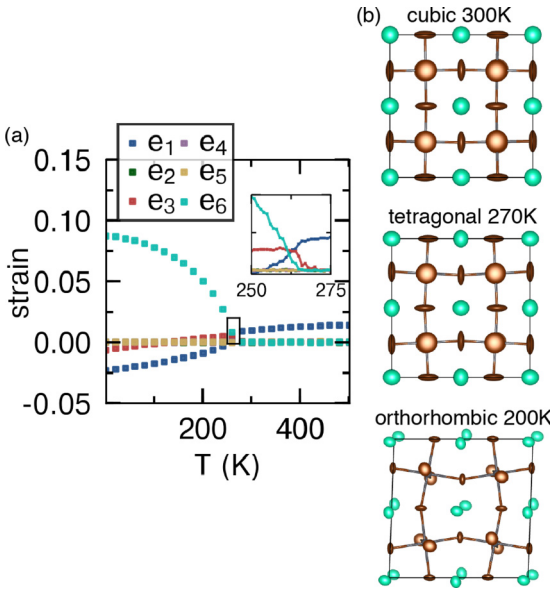

FIG. 6. (a) Thermodynamically averaged strain order parameters as calculated with Monte Carlo simulations applied to the anharmonic cluster expansion of Table I. (b) Thermodynamically averaged displacement covariances were used to compute the atomic displacement parameters (ADPs). The ADP ellipsoids enclose 90% of the cumulative probability density of atomic motion.

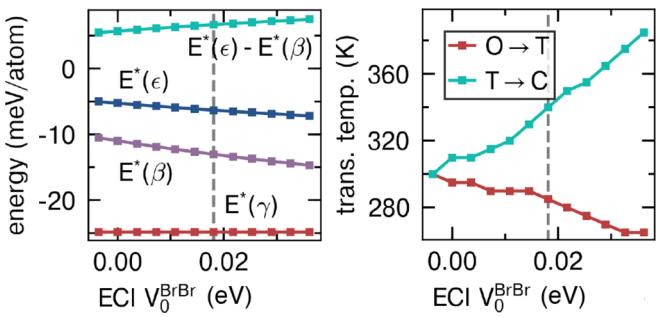

FIG. 7. (a) Energies of γ, β, and ϵ relative to undistorted α (set equal to zero) as a function of V_0^{BrBr} while keeping the relative values of all other coefficients of the anharmonic vibrational Hamiltonian of Table I constant (all Hamiltonian coefficients were rescaled to maintain a constant difference in energy between γ and α). (b) Transition temperatures as a function of V_0^{BrBr}. The temperature interval in which the tetragonal β phase is stable increases as the energies of β and ϵ decrease relative to those of γ. The dashed gray line indicates an effective cluster interaction (ECI) of 0.018 eV and is the model used to investigate local octahedral tilt environments.

Carlo simulations applied to the anharmonic cluster expansion of Table I. The strain order parameters, $e_1, \ldots, e_6$, are symmetry-adapted linear combinations of the Hencky strains measured relative to a cubic reference state of perovskite, with the Cartesian axes aligned parallel to the cubic perovskite primitive unit-cell vectors [58]. The first strain order parameter, e_1, measures shape-preserving volumetric change. The other five strain order parameters measure symmetry changes relative to the cubic reference and are zero in the cubic phase. The pair of order parameters (e_2, e_3) describes tetragonal and/or orthorhombic symmetry breaking, with e_3 describing tetragonal deformations along the z axis. The subspace (e_4, e_5, e_6) describes shear strain, with e_6 describing tetragonal-orthorhombic symmetry breaking relative to the z-oriented tetragonal phase. In short, the tetragonal phase β can be distinguished from the cubic phase by a nonzero e_3 order parameter, while the orthorhombic phase γ has nonzero e_3 and e_6 order parameters [20]. Figure 6 shows that the orthorhombic phase is predicted to be stable at low temperature where e_3 and e_6 differ from zero. At high temperature, the crystal adopts an average cubic structure as only the volumetric strain order parameter e_1 is nonzero. While it is not immediately evident from Fig. 6, the inset suggests a very narrow temperature interval centered at 270 K in which the tetragonal phase becomes stable, as manifested by a nonzero e_3.

In addition to tracking variations in average lattice parameters and symmetries with temperature, we can also analyze local atomic displacements. To this end, we collected thermodynamically averaged atomic coordinates and displacement covariance matrices, $U_{ij} = \langle u_i u_j \rangle - \langle u_i \rangle \langle u_j \rangle$, for each atom (where i and j represent Cartesian components of the atomic displacement vector $\vec{u}$). The displacement covariance matrices define an anisotropic Gaussian probability distribution for atomic displacements and are used to compute thermal ellipsoids at 90% probability contours in Fig. 6(d) for the observed orthorhombic, tetragonal, and cubic phases. The structures reproduce the tilt modes and A-cation displacements of the experimentally observed γ and α phases. Remarkably, the atomic displacement parameters show excellent qualitative agreement to those observed experimentally for the halide perovskite $CsSnBr_3$ [14]. In particular, the high-temperature cubic phase shows very large pancake-shaped Br atomic displacement parameters (ADPs), indicating a high degree of motion in only one plane. These correspond to large-amplitude and highly anharmonic lattice dynamics associated with octahedral tilting of the $PbBr_6$ inorganic sublattice.

C. Stabilizing the tetragonal phase

The anharmonic vibrational Hamiltonian of Table I, while reproducing the experimentally observed γ to β and the β to α structural phase transitions exhibited by many inorganic halide perovskites, stabilizes the tetragonal β phase in only a very narrow temperature interval (Fig. 6). Experimental studies of halide perovskites usually show a larger temperature interval in which the tetragonal phase is stable. It is possible to increase the predicted stability window of the tetragonal β phase by parametrically adjusting the expansion coefficients of the anharmonic vibrational Hamiltonian of Table I. Figure 7(a), for example, shows that the stability of β relative to γ and α can be enhanced by increasing the first-order term, V_0^{BrBr}, of the Br-Br pair-cluster function [i.e., V_0 in $\Phi_{\mathrm{BrBr}}(q_0) = V_0 q_0 + V_1 q_0^2$]. An increase in the value of V_0^{BrBr} has the effect of shifting the minimum in the Br-Br pair-cluster function to smaller distances relative to its reference distance in the cubic phase. As is clear from Fig. 7(b), increasing V_0^{BrBr} lowers the saddle-point energy of β relative to that of γ and α. It also lowers the energy of the other saddle point corresponding to the orthorhombic ϵ variant

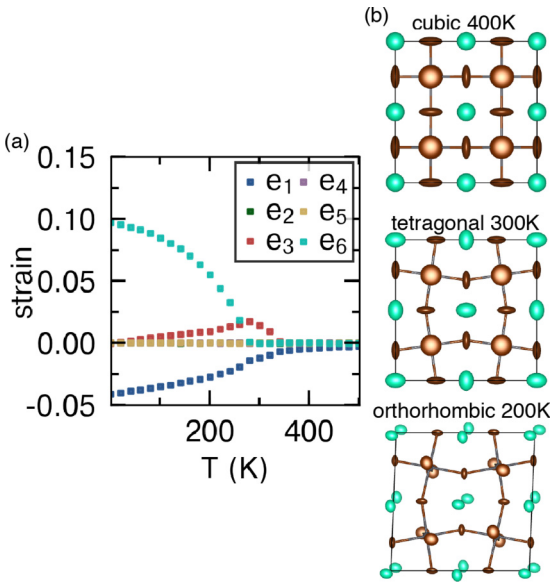

FIG. 8. (a) Thermodynamically averaged strain order parameters from Monte Carlo simulations using an anharmonic vibrational Hamiltonian that stabilizes the β phase over a wide temperature interval (see text for more details). Representative structures are shown in (b), along with thermodynamically averaged ADP ellipsoids, which enclose 90% of the cumulative probability density of atomic motion.

but slightly increases the gap between β and ϵ. In varying V_0^{BrBr} parametrically, we rescaled all other parameters of the anharmonic vibrational Hamiltonian such that the energy difference between γ and α remains constant. Monte Carlo simulations performed on supercells containing 1728 unit cells at 5-K temperature increments show that an increase in V_0^{BrBr} results in a divergence of the γ to β and the β to α transition temperatures, thereby widening the temperature interval in which β is stable [Fig. 7(b)].

Figure 8 shows thermodynamically averaged strain order parameters as calculated with an anharmonic vibrational Hamiltonian in which V_0^{BrBr} has a value corresponding to the dashed line in Fig. 7 and all other parameters of Table I are rescaled to maintain a constant energy difference between γ and α. Also shown in Fig. 8 is the average structure at different temperatures along with the ADPs derived from the thermodynamically averaged displacement covariance matrices. This reparametrized anharmonic vibrational Hamiltonian exhibits a much more robust range of stability for the tetragonal β phase. Both the orthorhombic and cubic phases show the same distinctive behavior as predicted by the original Hamiltonian of Table I; however, the tetragonal phase shows an additional anisotropy of the Cs displacements with a football-shaped thermal ellipsoid.

D. Octahedral tilts across transitions

The phase transitions in inorganic halide perovskites are often described in terms of the collective tilt modes of the halide sublattice. We explored the local environment due to octahedral tilts as shown in Fig. 9 with the anharmonic vibrational Hamiltonian used to calculate the properties of Fig. 8. At each temperature, we collected extrinsic Euler

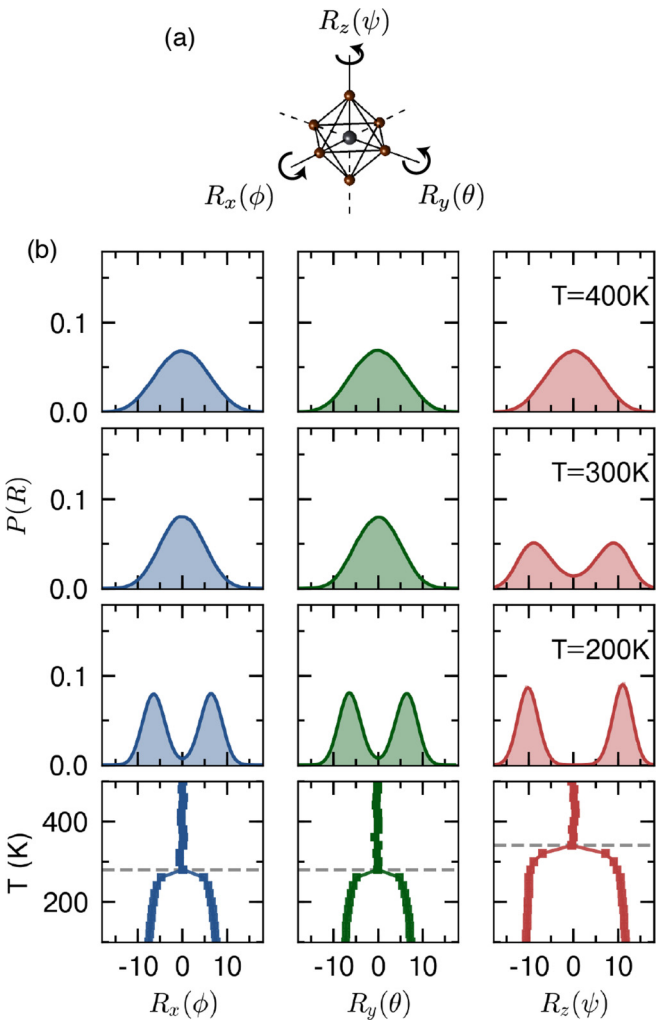

FIG. 9. (a) Diagram of the extrinsic Euler rotations about the x, y, and z rotation axes denoted by ψ, ϕ, and θ, respectively. Histograms of octahedral rotation angles are shown for (b) 400, (c) 300, and (d) 200 K, representing the distribution of tilts in the cubic, tetragonal, and orthorhombic phases, respectively. Histogram data was averaged for a $8 \times 8 \times 8$ simulation cell and fit with Gaussian kernel density estimation. (e) Order parameter plots show the maxima of the octahedral tilt histograms as a function of temperature. In the cubic to tetragonal transition, the tilts along x and y go to zero, while the tilts along z go to zero only during the tetragonal to cubic transition.

rotation angles for all octahedra in the simulation cell after every Monte Carlo pass. Euler angles were extracted by first applying the Kabsch algorithm to each octahedron to find the optimal rotation matrix that minimizes the squared distances between the deformed and reference octahedra. The rotation matrix was then decomposed into elementary extrinsic Euler angles, $R_x(\phi)$, $R_y(\theta)$, and $R_z(\psi)$, which represent rotations about the Cartesian x, y, and z axes, respectively.

Figure 9(b) shows histograms of the individual octahedral rotations in each phase. In the orthorhombic phase there exist bimodal peaks in the distribution for each Euler angle. In these simulations the in-phase rotation takes place about the z axis, while the out-of-phase rotations occur along the x and y axes. There is a progression in octahedral rotations between

the orthorhombic and tetragonal phases as the bimodal peaks along x and y combine to a single peak centered at zero in the tetragonal phase. Likewise, the in-phase tilting peaks coalesce into one peak centered at zero upon heating to the cubic phase. The distributions are shown as a function of temperature in Fig. 9(e), where the average rotation angles can serve as order parameters through the two phase transitions.

IV. DISCUSSION

The cubic and tetragonal forms of many halide perovskites are predicted to be dynamically unstable at zero Kelvin by DFT electronic structure methods. Nevertheless, these phases exist at finite temperature, often even at room temperature. The anharmonic vibrational Hamiltonians introduced in this study allow us to understand the finite temperature properties of halide perovskites. They faithfully reproduce important features of the energy surface of typical inorganic halide perovskites and are validated against a large database of first-principles energies for large-amplitude deformation states of $CsPbBr_3$ perovskite [51]. Remarkably, Monte Carlo simulations utilizing this Hamiltonian predict the thermodynamic stability of the cubic and tetragonal phases at elevated temperature, in spite of the fact that they are dynamically unstable at zero Kelvin.

The Monte Carlo simulations also enable characterization of local structural features as a function of temperature. The bimodal distribution of thermodynamically averaged octahedral tilt angles coalesce into one peak, centered at zero, upon passing through the tetragonal-cubic phase transition. Although the average octahedral rotation angles are zero in the cubic phase, their distributions indicate large local deviations from the high-symmetry phase. Hence our Monte Carlo simulations suggest that the material is on average cubic, but large octahedral tilt modes are still present, consistent with experimental observations [5]. Moreover, the calculated thermal ellipsoids qualitatively match those observed experimentally in similar halide-perovskite chemistries. These results suggest that anharmonic vibrational excitations play a determining role in the wide variety of electronic and mechanical properties of halide perovskites and should be explicitly accounted for when studying these properties.

The anharmonic vibrational Hamiltonian of the present study can be viewed as a cousin of other lattice Hamiltonians, such as the Ising model, the Heisenberg model, and the rigid rotor cluster expansion [59–66]. It is remarkable that the rich physics of structural phase transitions in perovskites due to octahedral tilts can be predicted with a Hamiltonian consisting of only an elastically deformable octahedron and four pair interactions. Although the interaction potential for the $PbBr_6$ octahedron is globally convex and nearly harmonic, the CsBr pair-cluster interaction shown in Fig. 4(a) has a minimum at a bond length that is shorter than in the reference cubic crystal. The low-temperature dynamical instability of the α and β phases thus appears to arise wholly due to pairs whose optimal bond length cannot be realized in either high-temperature phase, in qualitative agreement with perspectives on perovskite structural phase transitions based on the Goldschmidt tolerance factor. The parametrized Hamiltonian corresponds to a Goldschmidt tolerance factor that is less than 1 for $CsPbBr_3$, which indicates that the A-site cation (Cs in $CsPbBr_3$) is undersized and therefore undercoordinated in the cubic symmetry. Octahedral tilting occurs in the perovskites with a Goldschmidt factor less than 1 upon cooling in order to satisfy the coordination environment of the A-site cation.

While the anharmonic vibrational Hamiltonians of this work are capable of predicting the essential physics of the structural transitions of halide perovskites, further refinements of the Hamiltonian are possible. As an example, our parametric study of the anharmonic vibrational Hamiltonian indicates that a decrease in the optimal length of Br-Br pairs, achieved by increasing the first-order coefficient V_0^{BrBr}, enhances the stability of the tetragonal phase relative to the cubic phase. Other coefficients are likely to affect the sequence of octahedral tilt-phase transformations in different ways. The inclusion of more or higher-order cluster interactions may result in models that can capture more complex symmetry-breaking phenomena while also achieving higher fidelity to *ab initio* validation data. A higher-order interaction function for the $PbBr_6$ octahedron would be able to describe instabilities within the octahedron itself, for example, due to Pb off-centering. As presented, the minimal anharmonic Hamiltonian does not account for electrostatic interactions, which are important in more ionic crystals and tend to die off more slowly than those due to covalent bonds. These can be captured by adding longer-range pair clusters or by explicitly correcting for dipole-dipole interactions, which follow well-known functional forms in reciprocal space [67]. The qualitative changes in the phonon dispersion near Γ, such as LO-TO splitting, that result from explicit consideration of electrostatic effects have minimal impact on the phonon density of states and therefore on integrated properties such as free energies. Consequently, it is typically unnecessary to incorporate a rigorous electrostatic treatment in a model Hamiltonian to accurately predict thermodynamic equations of state. The minimal anharmonic Hamiltonian can also be combined with tight-binding Hamiltonians to develop a Hamiltonian that describes both electronic and anharmonic vibrational degrees of freedom. These are left to future studies.

V. CONCLUSIONS

In this work, we developed an anharmonic vibrational Hamiltonian based on descriptors of cluster deformations that is capable of capturing the qualitative features of tilt transitions in halide perovskites. The Hamiltonian is able to reproduce low-energy DFT configurations with a high degree of accuracy and qualitatively reproduce the energy landscape associated with octahedral tilts. Monte Carlo simulations showed that a minimal anharmonic vibrational Hamiltonian is capable of predicting the complex phase sequence of octahedral tilt modes in halide perovskites observed experimentally. The simulations demonstrated that the cubic and tetragonal forms of $CsPbBr_3$, which are predicted to be dynamically unstable at zero Kelvin, emerge at finite temperature as a result of large anharmonic vibrational excitations. An analysis of octahedral tilt statistics in Monte Carlo simulations shows that the cubic and tetragonal phases only adopt those symmetries on average, exhibiting large octahedral tilts around their average tilt angles. These results suggest the

importance of anharmonic vibrational excitations in determining the electronic, thermodynamic, and mechanical properties of room-temperature halide perovskites.

ACKNOWLEDGMENTS

This material is based upon work supported by the National Science Foundation, Grant No. OAC-1642433. Computational resources provided by the National Energy Research Scientific Computing Center (NERSC), supported by the Office of Science and US Department of Energy under Contract No. DE-AC02-05CH11231, are gratefully acknowledged, in addition to support from the Center for Scientific Computing from the CNSI, MRL, and NSF MRSEC (No. DMR-1720256).

[1] M. A. Green and A. Ho-Baillie, ACS Energy Lett. **2**, 822 (2017).
[2] F. Zheng, L. Z. Tan, S. Liu, and A. M. Rappe, Nano Lett. **15**, 7794 (2015).
[3] T. Etienne, E. Mosconi, and F. De Angelis, J. Phys. Chem. Lett. **7**, 1638 (2016).
[4] C. Motta, F. El-Mellouhi, S. Kais, N. Tabet, F. Alharbi, and S. Sanvito, Nat. Commun. **6**, 7026 (2015).
[5] A. N. Beecher, O. E. Semonin, J. M. Skelton, J. M. Frost, M. W. Terban, H. Zhai, A. Alatas, J. S. Owen, A. Walsh, and S. J. L. Billinge, ACS Energy Lett. **14**, 880 (2016).
[6] P. Azarhoosh, S. McKechnie, J. M. Frost, A. Walsh, and M. Van Schilfgaarde, APL Mater. **4**, 091501 (2016).
[7] D. Niesner, M. Wilhelm, I. Levchuk, A. Osvet, S. Shrestha, M. Batentschuk, C. Brabec, and T. Fauster, Phys. Rev. Lett. **117**, 126401 (2016).
[8] H. Zhu, K. Miyata, Y. Fu, J. Wang, P. P. Joshi, D. Niesner, K. W. Williams, S. Jin, and X.-Y. Zhu, Science **353**, 1409 (2016).
[9] X. Y. Zhu and V. Podzorov, J. Phys. Chem. Lett. **6**, 4758 (2015).
[10] H. Zhu, M. T. Trinh, J. Wang, Y. Fu, P. P. Joshi, K. Miyata, S. Jin, and X.-Y. Zhu, Adv. Mater. **29**, 1603072 (2017).
[11] C. C. Stoumpos, C. D. Malliakas, J. A. Peters, Z. Liu, M. Sebastian, J. Im, T. C. Chasapis, A. C. Wibowo, D. Y. Chung, A. J. Freeman, B. W. Wessels, and M. G. Kanatzidis, Cryst. Growth Des. **13**, 2722 (2013).
[12] L. Kubičár, V. Vretenár, and V. Boháč, Solid State Phenom. **138**, 3 (2008).
[13] M. Rodová and J. Brožek, J. Therm. Anal. **71**, 667 (2003).
[14] D. H. Fabini, G. Laurita, J. S. Bechtel, C. C. Stoumpos, H. A. Evans, A. G. Kontos, Y. S. Raptis, P. Falaras, A. Van der Ven, M. G. Kanatzidis, and R. Seshadri, J. Am. Chem. Soc. **138**, 11820 (2016).
[15] M. Mori and H. Saito, J. Phys. C: Solid State Phys. **19**, 2391 (1986).
[16] M. H. Kuok, E. L. Saw, and C. T. Yap, Phys. Status Solidi A **132**, K89 (1992).
[17] J.-C. Zheng, C. H. A. Huan, A. T. S. Wee, and M. H. Kuok, Surf. Interface Anal. **28**, 81 (1999).
[18] D. E. Scaife, P. F. Weller, and W. G. Fisher, J. Solid State Chem. **9**, 308 (1974).
[19] C. C. Stoumpos, C. D. Malliakas, and M. G. Kanatzidis, Inorg. Chem. **52**, 9019 (2013).
[20] J. S. Bechtel and A. Van der Ven, Phys. Rev. Mater. **2**, 025401 (2018).
[21] I. P. Swainson, C. Stock, S. F. Parker, L. Van Eijck, M. Russina, and J. W. Taylor, Phys. Rev. B **92**, 100303(R) (2015).
[22] A. Marronnier, H. Lee, B. Geffroy, J. Even, Y. Bonnassieux, and G. Roma, J. Phys. Chem. Lett. **8**, 2659 (2017).
[23] M. Sakata, J. Harada, M. J. Cooper, and K. D. Rouse, Acta Crystallogr. Sect. A **36**, 7 (1980).
[24] R. X. Yang, J. M. Skelton, E. L. da Silva, J. M. Frost, and A. Walsh, J. Phys. Chem. Lett. **8**, 4720 (2017).
[25] M. A. Carignano, S. A. Aravindh, I. S. Roqan, J. Even, and C. Katan, J. Phys. Chem. C **121**, 20729 (2017).
[26] A. M. Glazer, Acta Crystallogr. Sect. B **28**, 3384 (1972).
[27] O. Sugino and R. Car, Phys. Rev. Lett. **74**, 1823 (1995).
[28] X. Wang, S. Scandolo, and R. Car, Phys. Rev. Lett. **95**, 185701 (2005).
[29] M. Kaczmarski, O. N. Bedoya-Martínez, and E. R. Hernández, Phys. Rev. Lett. **94**, 095701 (2005).
[30] O. Hellman, I. A. Abrikosov, and S. I. Simak, Phys. Rev. B **84**, 180301(R) (2011).
[31] A. van de Walle, Q. Hong, S. Kadkhodaei, and R. Sun, Nat. Commun. **6**, 7559 (2015).
[32] S. Kadkhodaei, Q.-J. Hong, and A. van de Walle, Phys. Rev. B **95**, 064101 (2017).
[33] K. M. Rabe and J. D. Joannopoulos, Phys. Rev. Lett. **59**, 570 (1987).
[34] K. M. Rabe and U. V. Waghmare, Ferroelectrics **136**, 147 (1992).
[35] W. Zhong, D. Vanderbilt, and K. M. Rabe, Phys. Rev. Lett. **73**, 1861 (1994).
[36] K. Rabe and U. Waghmare, J. Phys. Chem. Solids **57**, 1397 (1996).
[37] K. M. Rabe and U. V. Waghmare, Phys. Rev. B **52**, 13236 (1995).
[38] W. Zhong, D. Vanderbilt, and K. M. Rabe, Phys. Rev. B **52**, 6301 (1995).
[39] K. M. Rabe and U. V. Waghmare, Ferroelectrics **164**, 15 (1995).
[40] W. Zhong, D. Vanderbilt, R. D. King-Smith, and K. Rabe, Ferroelectrics **164**, 291 (1995).
[41] K. M. Rabe and U. V. Waghmare, Philos. Trans. R. Soc., A **354**, 2897 (1996).
[42] U. V. Waghmare and K. M. Rabe, Phys. Rev. B **55**, 6161 (1997).
[43] E. Cockayne and K. M. Rabe, Phys. Rev. B **56**, 7947 (1997).
[44] U. V. Waghmare and K. M. Rabe, Ferroelectrics **194**, 135 (1997).
[45] K. M. Rabe and U. V. Waghmare, Ferroelectrics **194**, 119 (1997).
[46] J. Bhattacharya and A. Van der Ven, Acta Mater. **56**, 4226 (2008).
[47] J. C. Thomas and A. Van der Ven, Phys. Rev. B **88**, 214111 (2013).
[48] X. Ai, Y. Chen, and C. A. Marianetti, Phys. Rev. B **90**, 014308 (2014).

[49] J. C. Wojdeł, P. Hermet, M. P. Ljungberg, P. Ghosez, and J. Íñiguez, J. Phys.: Condens. Matter **25**, 305401 (2013).
[50] K. Momma and F. Izumi, J. Appl. Crystallogr. **44**, 1272 (2011).
[51] J. C. Thomas, J. S. Bechtel, A. R. Natarajan, and A. Van der Ven, Phys. Rev. B **100**, 134101 (2019).
[52] See Supplemental Material at http://link.aps.org/supplemental/10.1103/PhysRevMaterials.3.113605 for detailed definitions of the octahedral CCD variables, including the geometry of the undeformed reference cluster.
[53] This dataset comprised deformed structures of $CsPbBr_3$ obtained by applying a wide range of homogeneous strains and atomic displacements and their corresponding energies, as calculated with density functional theory (DFT). The Vienna Ab Initio Simulation Package (VASP) was used to carry out DFT calculations [68,69]. For all calculations, the GGA-PBESol functional was employed with projector augmented wave pseudopotentials and a 400-eV cutoff for the plane-wave basis set [68,70,71]. A $6 \times 6 \times 6$ Γ-centered k-point mesh was used for the perovskite unit cell, which resulted in energy convergence to within 1 meV/atom.
[54] CASM Developers, CASMCODEv0.2.1 (2017).
[55] A. Van der Ven, J. Thomas, Q. Xu, and J. Bhattacharya, Math. Comput. Simul. **80**, 1393 (2010).
[56] B. Puchala and A. Van der Ven, Phys. Rev. B **88**, 094108 (2013).
[57] J. C. Thomas and A. Van der Ven, Phys. Rev. B **90**, 224105 (2014).
[58] S. T. John and G. Csányi, J. Phys. Chem. B **121**, 10934 (2017).
[59] E. Ising, Z. Phys. **31**, 253 (1925).
[60] J. M. Sanchez, F. Ducastelle, and D. Gratias, Physica A **128**, 334 (1984).
[61] R. B. Potts, Math. Proc. Cambridge Philos. Soc. **48**, 106 (1952).
[62] J. Ashkin and E. Teller, Phys. Rev. **64**, 178 (1943).
[63] Y.-H. Li and S. Teitel, Phys. Rev. B **40**, 9122 (1989).
[64] R. Drautz and M. Fähnle, Phys. Rev. B **72**, 212405 (2005).
[65] J. C. Thomas, J. S. Bechtel, and A. Van der Ven, Phys. Rev. B **98**, 094105 (2018).
[66] A. Van der Ven, J. Thomas, B. Puchala, and A. Natarajan, Annu. Rev. Mater. Res. **48**, 27 (2018).
[67] N. W. Ashcroft and N. D. Mermin, *Solid State Physics* (Saunders College Publishing, Orlando, FL, 1976).
[68] G. Kresse and J. Furthmüller, Phys. Rev. B **54**, 11169 (1996).
[69] G. Kresse and D. Joubert, Phys. Rev. B **59**, 1758 (1999).
[70] J. P. Perdew, A. Ruzsinszky, G. I. Csonka, O. A. Vydrov, G. E. Scuseria, L. A. Constantin, X. Zhou, and K. Burke, Phys. Rev. Lett. **100**, 136406 (2008).
[71] P. E. Blöchl, Phys. Rev. B: Condens. Matter **50**, 17953 (1994).